JACS JOURNAL OF THE AMERICAN CHEMICAL SOCIETY

Article

Cite This: J. Am. Chem. Soc. 2019, 141, 15641−15648

pubs.acs.org/JACS

Synthesis and Properties of a Compositional Series of MIL-53(Al) Metal−Organic Framework Crystal-Glass Composites

Christopher W. Ashling,[†] Duncan N. Johnstone,[†] Remo N. Widmer,[‡] Jingwei Hou,[†] Sean M. Collins,[†] Adam F. Sapnik,[†] Alice M. Bumstead,[†] Paul A. Midgley,[†] Philip A. Chater,[§] David A. Keen,[∥] and Thomas D. Bennett*[,†]

[†]Department of Materials Science and Metallurgy, University of Cambridge, Cambridge, CB3 0FS U.K.

[‡]Department of Earth Sciences, University of Cambridge, Downing Street, Cambridge, CB2 3EQ U.K.

[§]Diamond Light Source Ltd., Diamond House, Harwell Campus, Didcot, Oxfordshire OX11 0DE U.K.

[∥]ISIS Facility, Rutherford Appleton Laboratory, Harwell Campus, Didcot, Oxfordshire OX11 0QX U.K.

Supporting Information

ABSTRACT: Metal−organic framework crystal-glass composites (MOF-CGCs) are materials in which a crystalline MOF is dispersed within a MOF glass. In this work, we explore the room-temperature stabilization of the open-pore form of MIL-53(Al), usually observed at high temperature, which occurs upon encapsulation within a ZIF-62(Zn) MOF glass matrix. A series of MOF-CGCs containing different loadings of MIL-53(Al) were synthesized and characterized using X-ray diffraction and nuclear magnetic resonance spectroscopy. An upper limit of MIL-53(Al) that can be stabilized in the composite was determined for the first time. The nanostructure of the composites was probed using pair distribution function analysis and scanning transmission electron microscopy. Notably, the distribution and integrity of the crystalline component in a sample series were determined, and these findings were related to the MOF-CGC gas adsorption capacity in order to identify the optimal loading necessary for maximum CO_2 sorption capacity.

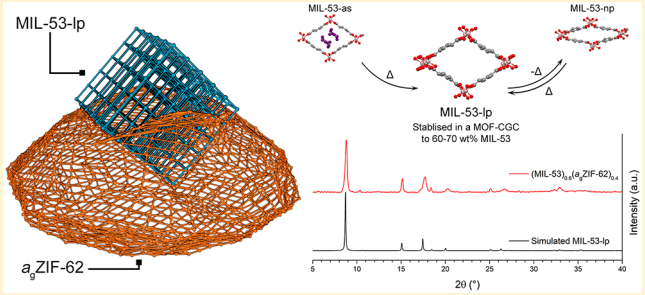

INTRODUCTION

Metal−organic frameworks (MOFs) are hybrid framework materials containing metal nodes that are linked in an extended fashion by organic molecules.[1] MOFs are highly regarded for their record-breaking surface areas and tunable pore sizes[2,3] and are investigated for a plethora of applications including gas storage and separation, catalysis, water harvesting, and sensing.[1,4−7] The exploitation of the full *chemical* promise of MOFs in practice may however be impeded by their *physical* form. Typically, MOFs are synthesized as microcrystalline powders of nanometer- to millimeter-sized particles that are ill-suited to industrial settings without prior processing.[8] This has driven attempts to synthesize bulk materials (monoliths) using techniques such as sol−gel synthesis[9−11] and postsynthetic compaction and pelletization via, for example, spark-plasma sintering.[12,13] Most MOF monolith research has, however, used a secondary material to aggregate the MOF crystallites such as in MOF-in-silica and mixed-matrix membrane systems.[14,15]

Zeolitic imidazolate frameworks (ZIFs) are a subfamily of MOFs and have been proven to be particularly suitable candidates for the synthesis of MOF monoliths. ZIFs are defined by their incorporation of imidazolate or imidazolate-based linkers and are notable among MOFs for their high thermal stabilities (ca. 300−500 °C).[16−18] The incorporation of these bidentate linkers leads ZIFs to adopt many topologies identical to those of zeolites because the metal−imidazolate−metal dihedral angle is similar to that of silicon−oxygen−silicon (∼145°).[16] Several ZIFs have been observed to undergo melting, forming extremely viscous MOF liquids at high temperatures, which can be quenched to form glasses.[19] Structurally, the glass displays the same short-range order and stoichiometry of the crystalline material (i.e., the metal nodes retain a tetrahedral coordination with a connectivity that can be modeled as a continuous random network (CRN)).[20]

The glassy state of MOFs has been used to create MOF crystal-glass composites (MOF-CGCs), in which a crystalline phase is incorporated into a MOF−glass matrix.[21] The first example of such a material was synthesized by forming a physical mixture of crystalline MIL-53(Al) [Al(OH)(bdc)] (bdc, 1,4-benzenedicarboxylate, $C_8H_4O_4^{2-}$), hereafter referred to as MIL-53, and ZIF-62(Zn) [$Zn(Im)_{1.75}(bIm)_{0.25}$] (Im, imidazolate, $C_3N_2H_3^-$; bIm, benzimidazolate, $C_7H_5N_2^-$), hereafter referred to as ZIF-62.[21] This mixture was heated above the melting temperature of ZIF-62 and cooled to room

Received: July 18, 2019
Published: September 6, 2019

DOI: 10.1021/jacs.9b07557
J. Am. Chem. Soc. 2019, 141, 15641−15648

temperature to form the MOF-CGC $(MIL\text{-}53)_{0.25}(a_gZIF\text{-}62)_{0.75}$, (i.e., a MOF-CGC composed of 25 wt% MIL-53 in a_gZIF-62, where a_g denotes the glassy form).

MIL-53 crystallizes in a "wine rack" structure (*Pnma*, a = 17.129(2) Å, b = 6.628(1) Å, c = 12.182(1) Å, $\alpha = \beta = \gamma = 90°$) with large internal pores held open by excess solvent and unreacted ligand in the as-synthesized state (MIL-53-as).[22] The removal or replacement of these guest molecules can cause the pore structure to undergo significant volume contraction or expansion, leading to phase transformations at different temperatures (Figure 1a). When the pore-occupying

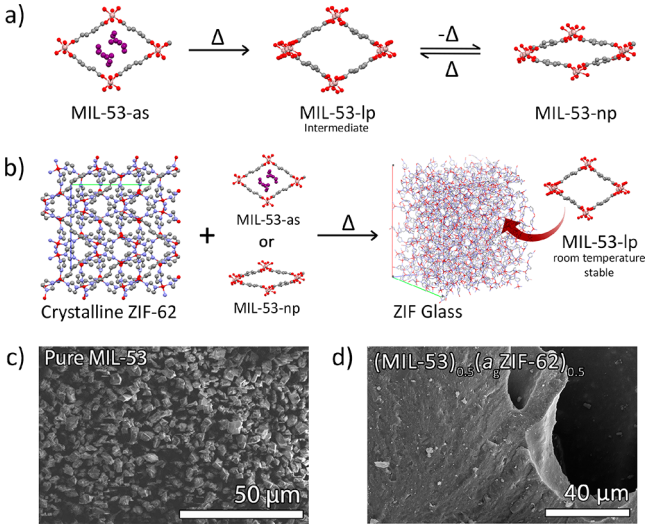

Figure 1. (a) Diagram of the activation process of MIL-53 and the transition between different states (C, gray; O, red; Al, pink; H, omitted for clarity; solvent, purple). (b) Schematic of composite formation using ball-and-stick figures of MIL-53, crystalline ZIF-62 (N, blue; Zn, red), and the reverse Monte Carlo (RMC) model using combined X-ray and neutron total scattering data of a_gZIF-4 [$Zn(Im)_2$].[19] (c) Scanning electron microscopy image (SEM) of MIL-53-as from Hou et al.[21] (d) Scanning electron microscope (SEM) image of $(MIL\text{-}53)_{0.5}(a_gZIF\text{-}62)_{0.5}$.

species are expelled, typically by heating, an open-pore structure (*Imma*, a = 6.608(1) Å, b = 16.675(3) Å, c = 12.813(2) Å, $\alpha = \beta = \gamma = 90°$) is formed with a greater internal void volume that we refer to as MIL-53-lp (large pore). The spontaneous uptake of water into the large-pore phase, typically upon cooling, causes the pores to contract to produce a narrow-pore structure (*Cc*, a = 19.513(2) Å, b = 7.612(1) Å, c = 6.576(1) Å, $\alpha = \gamma = 90°$, β = 104.24(1)°) that we refer to as MIL-53-np (narrow pore).[22] Reversible transitions between MIL-53-np and MIL-53-lp are known as breathing.

It was recently observed that when incorporated into a MOF-CGC, the MIL-53-lp structure was stabilized at room temperature (Figure 1b), and because of the greater pore space compared to that of MIL-53-np, the $(MIL\text{-}53)_{0.25}(a_gZIF\text{-}62)_{0.75}$ CGC displayed a CO_2 uptake greater than a combination of its parent materials.[21] Motivated by this potential for composite formation to enhance gas sorption and to achieve the designed stabilization of an open pore structure, we study here the maximum loading capacity of MIL-53 within a $(MIL\text{-}53)_x(a_gZIF\text{-}62)_{1-x}$ series. Various characterization techniques are used to probe the chemical composition and structural integrity of the MOF-CGC components across the $(MIL\text{-}53)_x(a_gZIF\text{-}62)_{1-x}$ series, and we pay particular attention to the MIL-53 phases present.

RESULTS AND DISCUSSION

Synthesis of MOF-CGC Series and Retention of MIL-53-lp. Samples of $(MIL\text{-}53)_x(a_gZIF\text{-}62)_{1-x}$, where x = 0.25, and also $0.3 \leqslant x \leqslant 0.9$ in 0.1 increments, were synthesized by ball milling appropriate masses of crystalline ZIF-62 and MIL-53-as, pressing the resultant intimately mixed powder in a 13-mm-diameter dye at 0.74 GPa, heating to 450 °C for 15 min, and quenching to room temperature (Methods). The materials produced were opaque, cream-colored monoliths, which became brown with increasing concentrations of MIL-53, ascribed to a small amount of thermal decomposition of the MIL-53 component. Neither parent material can be identified from SEM images, and the relatively smooth surfaces of the bulk material provide evidence of appreciable flow in the ZIF-62 liquid state (Figures 1c,d and S1−S5).

To verify that the stabilization of MIL-53-lp in $(MIL\text{-}53)_x(a_gZIF\text{-}62)_{1-x}$ CGCs is not related to the presence of occluded ligand within MIL-53-as during CGC formation, a CGC was prepared using MIL-53-np as the starting material. The MIL-53-np phase was obtained by heating a sample of pure MIL-53-as to 330 °C for 72 h to produce MIL-53-lp, which was then cooled to room temperature and underwent the reported phase transition to MIL-53-np (Figures 1, 2, and

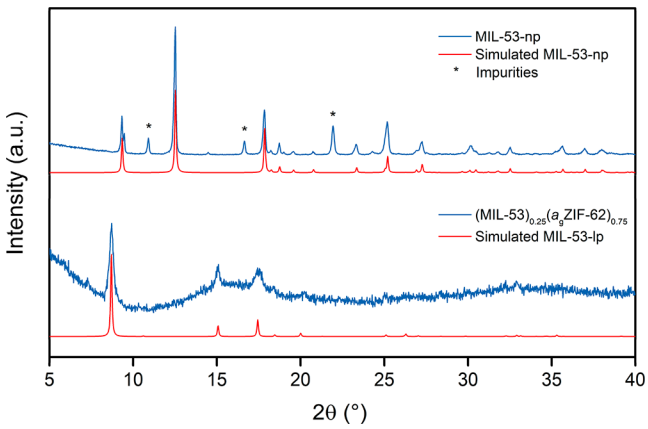

Figure 2. Experimental PXRD patterns (blue) of pure MIL-53-np (top) and the CGC (bottom). The simulated patterns (red) demonstrates the retention of the MIL-53-lp phase in quenched CGCs. Impurities marked with * have also been observed in the literature.[23]

S6). A $(MIL\text{-}53)_{0.25}(a_gZIF\text{-}62)_{0.75}$ CGC was then produced (Methods section) using this MIL-53-np starting material and was left in an unsealed container under ambient conditions for 24 h before lab-source powder X-ray diffraction (PXRD) data were collected (Methods section). The experimental pattern displays agreement with the simulated pattern for MIL-53-lp and is dissimilar to MIL-53-np (Figure 2). This demonstrates that the dominant MIL-53 phase present within $(MIL\text{-}53)_{0.25}(a_gZIF\text{-}62)_{0.75}$ is MIL-53-lp regardless of the starting phase. Further composite synthesis reported here was performed using MIL-53-as as the starting material.

Composition, MIL-53 Phase Identification, and Loading Capacity. The integrity and retention of organic linkers in MOF-CGCs across the composition series were studied using solution ^{1}H nuclear magnetic resonance (NMR) (Methods

DOI: 10.1021/jacs.9b07557
J. Am. Chem. Soc. 2019, 141, 15641−15648

section). The presence of peaks assignable to HIm, HbIm, and H_2bdc confirmed that the organic linkers present in crystalline ZIF-62 and MIL-53 were also present in all composites (Figure 3a). A ratio of 1:6.93 between peak intensities corresponding

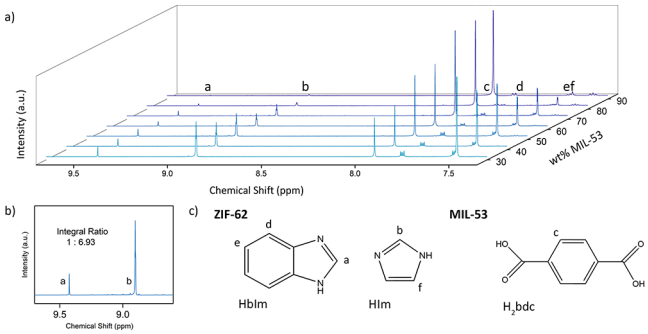

Figure 3. (a) ^{1}H NMR spectra of the $(\text{MIL-53})_x(a_g\text{ZIF-62})_{1-x}$ MOF-CGC series using a 2.5:1 ratio of deuterated dimethyl sulfoxide and hydrochloric acid solvents. (b) Peak integral ratios for organic ligands in $(\text{MIL-53})_{0.25}(a_g\text{ZIF-62})_{0.75}$. (c) Ligands within the frameworks. Peaks in the NMR spectra (a) are assigned (a–f) to protons in the ligands as indicated in (c).

to benzimidazole and imidazole, respectively, is observed, confirming that there was no change in ZIF-62 stoichiometry upon glass formation (Figure 3b). The single expected signal arising from H_2bdc is observed to increase, while those assigned to HIm and HbIm decrease, as the content of MIL-53 is increased across the MOF-CGC series (Figure 3a).

Laboratory PXRD measurements (Cu Kα radiation, λ = 1.5418 Å) were carried out on the compositional series of finely ground $(\text{MIL-53})_x(a_g\text{ZIF-62})_{1-x}$ samples (Figure 4).

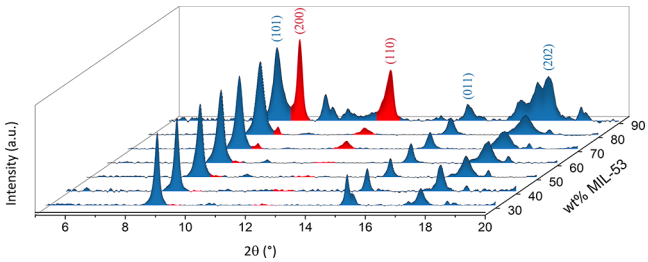

Figure 4. Laboratory powder X-ray diffraction patterns of the $(\text{MIL-53})_x(a_g\text{ZIF-62})_{1-x}$ composite series, highlighting the MIL-53-np Bragg reflections in red. Background subtracted for clarity and normalized to the (101) peak of MIL-53-lp (blue).

The diffraction pattern for $(\text{MIL-53})_{0.3}(a_g\text{ZIF-62})_{0.7}$ contained several peaks ascribed to the MIL-53-lp phase, of which the (101), (011), and (202) reflections were most prominent. No reflections were observed which could be ascribed to the MIL-53-np phase. However, upon increasing concentration of MIL-53 within the composite to 70 wt%, peaks ascribed to the (200) and (110) reflections of MIL-53-np phase emerged and increased in relative intensity thereafter. Subsequently, room-temperature X-ray total scattering data were collected for samples of the $(\text{MIL-53})_x(a_g\text{ZIF-62})_{1-x}$ series (and the corresponding crystalline mixtures of the same proportions) using synchrotron radiation (λ = 0.161669 Å, Methods section). These data display the rise of a peak emerging at 1.3 Å^{-1} for sample compositions of 70 wt % MIL-53 and above (Figure S7). This peak corresponds to the formation of the MIL-53-np phase and is in agreement with laboratory PXRD measurements. For greater phase determination accuracy, Rietveld refinement was performed on the synchrotron-source total scattering data using MIL-53-lp and MIL-53-np crystallographic information files (Table 1, Figures S7–S14).[22] The threshold for MIL-53-lp stabilization, using the materials processing described here, was therefore identified as between 60 and 70 wt% MIL-53. Higher incorporations led to the emergence of MIL-53-np.

Crystal-Glass Composite Microstructure. Scanning transmission electron microscopy (STEM) was used to investigate the microstructure in the $(\text{MIL-53})_x(a_g\text{ZIF-62})_{1-x}$ CGCs (Figure 5). Scanning electron diffraction (SED) was used to map the number of Bragg diffraction peaks measured in the diffraction pattern recorded at each probe position, as the electron probe was scanned across the sample, to reveal the location of the crystalline phases in MOF-CGCs, as shown in Figures 5c and S15–S17. These crystallinity maps demonstrate close contact between crystalline and noncrystalline regions within the MOF-CGCs across the composition range. Comparison with compositional maps showing the distribution of metal centers, obtained via STEM X-ray energy-dispersive spectroscopy (STEM-EDS) mapping of the same particles and shown in Figures 5a and S15–S17, confirms that the crystalline regions correspond to those which are rich in Al metal centers, as expected for MIL-53.

Pair distribution function (PDF) analysis is emerging as a powerful tool for investigating interatomic distances in crystalline and amorphous MOFs.[24−26] This technique yields atom–atom correlation histograms, which effectively indicate distances within a sample and provide information on structure, regardless of crystallinity. Structure factors, $S(Q)$, were obtained from processing the total scattering data of both the $(\text{MIL-53})_x(a_g\text{ZIF-62})_{1-x}$ samples and the corresponding crystalline mixtures, (MIL-53)(ZIF-62)(X/Y) where X and Y represent the respective weight percentages of the components. Those for the (MIL-53)(ZIF-62)(X/Y) series contain the Bragg scattering expected from both ZIF-62 and MIL-53, whereas structure factors from the $(\text{MIL-53})_x(a_g\text{ZIF-62})_{1-x}$ samples contain only that from MIL-53 (Figures S18–S26). Appropriate corrections were performed with the GudrunX software, and the data were Fourier transformed to obtain the corresponding PDFs.[27]

The intensity of the peaks in the PDFs of (MIL-53)(ZIF-62)(X/Y) varies proportionally between the two end members (MIL-53-as and crystalline ZIF-62) as a function of the relative proportions of each end member. This is unlike the PDFs of the $(\text{MIL-53})_x(a_g\text{ZIF-62})_{1-x}$ series which do not display the same ideal conformity between the end members of the series. This is likely due to (i) mixtures of MIL-53-np and MIL-53-lp phases and (ii) possible interactions at the interfaces between the crystal and glass (Figure 6). A comparison of the PDFs of (MIL-53)(ZIF-62)(X/Y) and $(\text{MIL-53})_x(a_g\text{ZIF-62})_{1-x}$ shows that correlations ascribed to the short-range order of ZIF-62 are retained after vitrification (Figure 6a peaks **1**–**5**). These peaks may be assigned to C–C (1.38 Å, **1**), Zn–N (1.98 Å, **2**), Zn–C (3.02 Å, **3**), Zn–N (4.18 Å, **4**), and Zn–Zn (5.96 Å, **5**) interatomic distances. In the composites, correlations above 6 Å ascribed to ZIF-62 tend to zero because of the loss of long-range order. Interatomic distances associated with MIL-53 may be identified in both series (Figure 6a, peaks a and b)—these peaks are assigned to Al–C (4.71 Å, a) and Al–Al (6.57 Å, b) interatomic distances—though they are noticeably less intense

DOI: 10.1021/jacs.9b07557
J. Am. Chem. Soc. 2019, 141, 15641−15648

Table 1. Crystallographic Data Determined from Rietveld Analyses of Total Scattering Data of the $(MIL\text{-}53)_x(a_gZIF\text{-}62)_{1-x}$ X-ray Diffraction Series[a]

	MIL-53-lp				MIL-53-np				
sample	a (Å)	b (Å)	c (Å)	quantity (%)	a (Å)	b (Å)	c (Å)	β (deg)	quantity (%)
MIL-53-lp[b]	**6.608(1)**	**16.675(3)**	**12.813(2)**						
MIL-53-np[b]					**19.513(2)**	**7.612(1)**	**6.576(1)**	**104.241(1)**	
$(MIL\text{-}53)_{0.3}(a_gZIF\text{-}62)_{0.7}$	6.59(1)	16.9(1)	12.65(5)	100					0
$(MIL\text{-}53)_{0.4}(a_gZIF\text{-}62)_{0.6}$	6.61(2)	16.7(2)	12.71(9)	100					0
$(MIL\text{-}53)_{0.5}(a_gZIF\text{-}62)_{0.5}$	6.64(2)	17.0(1)	12.46(6)	100					0
$(MIL\text{-}53)_{0.6}(a_gZIF\text{-}62)_{0.4}$	6.64(2)	17.0(1)	12.44(4)	100					0
$(MIL\text{-}53)_{0.7}(a_gZIF\text{-}62)_{0.3}$	6.64(2)	16.9(3)	12.55(13)	60(5)	19.22(10)	7.80(4)	6.82(5)	107.5(6)	40(5)
$(MIL\text{-}53)_{0.8}(a_gZIF\text{-}62)_{0.2}$	6.63(2)	16.8(3)	12.63(11)	55(5)	19.37(11)	7.73(3)	6.91(4)	106.2(4)	45(5)
$(MIL\text{-}53)_{0.9}(a_gZIF\text{-}62)_{0.1}$	7.02(6)	16.5(1)	12.74(8)	30(5)	19.37(7)	7.83(2)	6.84(4)	105.8(5)	70(5)

[a]Rietveld refinement plots are shown in Figures S7–S14. [b]Published data by Loiseau et al.[22]

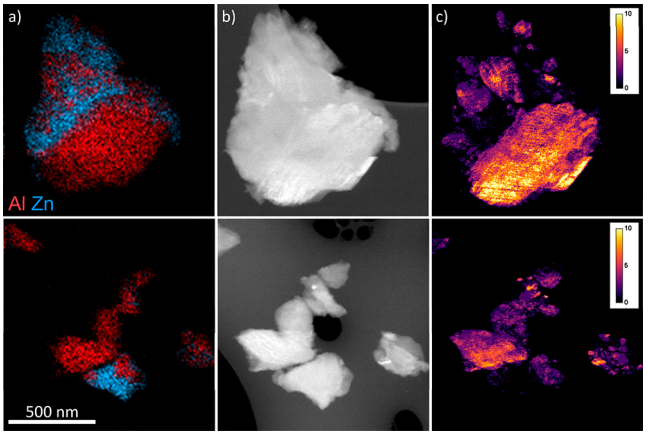

Figure 5. Scanning transmission electron microscopy of MOF-CGC particles from $(MIL\text{-}53)_{0.6}(a_gZIF\text{-}62)_{0.4}$ (upper) and $(MIL\text{-}53)_{0.9}(a_gZIF\text{-}62)_{0.1}$ (lower) samples. (a) Compositional maps of Al (red) and Zn (blue) metal centers from STEM-EDS mapping. (b) Annular dark-field images. (c) Crystallinity maps showing the number of Bragg peaks as a function of probe position in SED data. The color intensity scale for the crystallinity maps showing the number of Bragg scattering peaks identified at each probe position in the scanned field of view is presented for reference. Bragg peaks are recorded only from crystalline material, and the number of peaks recorded at each position depends on the local crystal orientation. The scale is identical for all images.

because of weaker scattering of Al compared to that of Zn. In the composite series, all correlations past the short-range order of ZIF-62 (~8 Å) originate from crystalline MIL-53. Predicted PDFs for ZIF-62, MIL-53-as, MIL-53-np, and MIL-53-lp with their corresponding metal–metal and metal–(N or O) are provided in Supporting Information Figures S27–S30.

The PDF of $(MIL\text{-}53)_{0.9}(a_gZIF\text{-}62)_{0.1}$ contains correlations at 10 and 14.5 Å, which qualitatively agree with peak positions in a predicted PDF for MIL-53-np (Figure S31). These are absent in the experimental PDF of MIL-53-as. The identification of the MIL-53-np phase within $(MIL\text{-}53)_{0.9}(a_gZIF\text{-}62)_{0.1}$ agrees with the PXRD data collected. We note that the PDFs of $(MIL\text{-}53)_{0.8}(a_gZIF\text{-}62)_{0.2}$ and $(MIL\text{-}53)_{0.7}(a_gZIF\text{-}62)_{0.3}$ do not display readily distinguishable MIL-53-np PDF correlations belonging to MIL-53-np. This may imply that an insufficient concentration of the MIL-53-np phase is present in these samples to give rise to such correlations, especially considering that the peak at 10 Å corresponds to a minimum in the PDFs from MIL-53-lp and MIL-53-as.

Bulk Structure and Properties. A sample of $(MIL\text{-}53)_{0.25}(a_gZIF\text{-}62)_{0.75}$ was previously observed to possess a CO_2 gas uptake of 66% of that of a pure sample of MIL-53-np.[21] Given that (i) MIL-53-lp is the main contributor to the adsorption capacity and (ii) the phase of MIL-53 remains unaltered to loadings of ⩽60 wt%, the adsorption capacities are expected to increase across those composites displaying only the MIL-53-lp phase. Changes in adsorption trends are, however, expected on moving to compositions above 60 wt% (i.e., the emergence of the MIL-53-np phase). The relationship between MIL-53 loading and gas uptake properties was probed using CO_2 gas adsorption isotherms for the full compositional series of MOF-CGCs (Figure 7, full isotherms in Figure S32).

For the samples of $(MIL\text{-}53)_{0.25}(a_gZIF\text{-}62)_{0.75}$–$(MIL\text{-}53)_{0.6}(a_gZIF\text{-}62)_{0.4}$, the total CO_2 quantity that is adsorbed increases in a broadly linear fashion, from 1.06 to 2.55 mmol/g, in accordance with the increasing concentration of MIL-53 in these samples, which is all present in the MIL-53-lp phase. A direct comparison of the gas sorption capacity of pure MIL-53-lp is not possible because the phase is unstable under the (room-temperature) conditions used for gas adsorption measurement of these composites. Furthermore, any high-temperature study on MIL-53-lp provides a poor comparison given the temperature dependence of gas adsorption.

$(MIL\text{-}53)_{0.7}(a_gZIF\text{-}62)_{0.3}$ and $(MIL\text{-}53)_{0.8}(a_gZIF\text{-}62)_{0.2}$ also display successively higher CO_2 adsorption. These two samples possess comparable amounts of MIL-53-lp, though the greater proportion of MIL-53 compared to that of a_gZIF-62 in the latter sample renders its total CO_2 uptake higher. A significant decline in capacity is observed for $(MIL\text{-}53)_{0.9}(a_gZIF\text{-}62)_{0.1}$ because this material primarily comprises the MIL-53-np phase. Pure samples of MIL-53-np and a_gZIF-62 display CO_2 adsorption capacities of 1.99 and 0.79 mmol/g, respectively (at 273 K at 1 bar, Figure 7). Furthermore, the sorption capacity of MIL-53-as is expected to be far lower than that of MIL-53-np because of the pore occupying species. Hence, compared to the room-temperature stable forms of the pure MIL-53 (i.e., MIL-53-np and MIL-53-as), the composite has the greatest CO_2 capacity under ambient conditions. We also note that, as observed by Hou et al.,[21] mesopores are expected in all of the composites, which will enhance the CO_2 uptake capacity.

■ CONCLUSIONS

In this study, we have synthesized a compositional series of $(MIL\text{-}53)_x(a_gZIF\text{-}62)_{1-x}$ crystal-glass composites. Sample

DOI: 10.1021/jacs.9b07557
J. Am. Chem. Soc. 2019, 141, 15641–15648

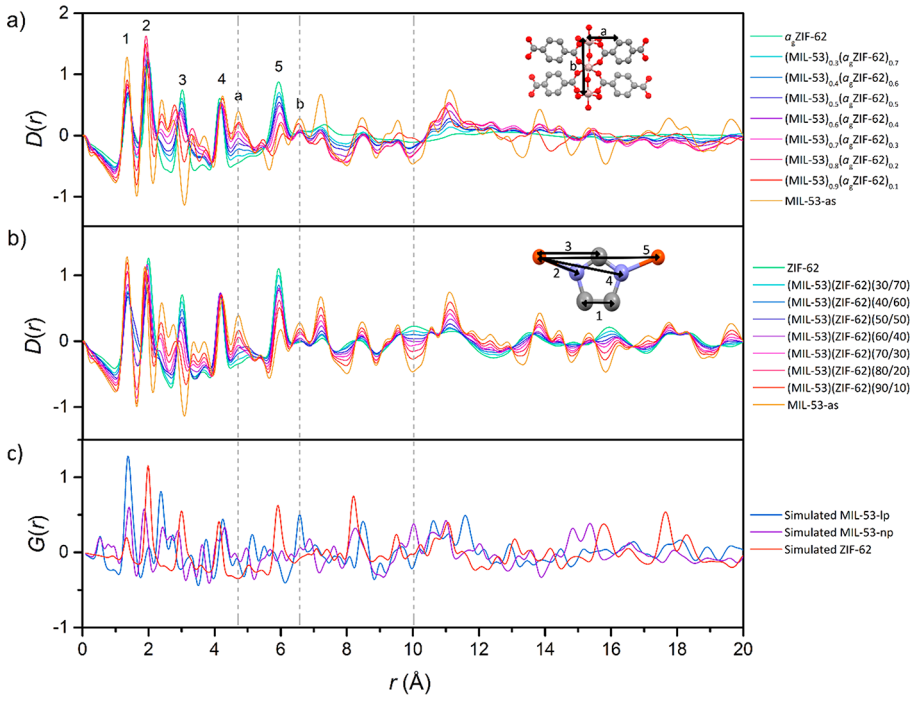

Figure 6. (a) Overlay PDFs of the $(MIL\text{-}53)_x(a_gZIF\text{-}62)_{1-x}$ series with a_gZIF-62, MIL-53-as—MIL-53-as, and MIL-53-lp are structurally similar, and MIL-53-lp is unstable at room temperature. (Inset) MIL-53-lp (Al, pink; O, red; C, gray) with correlation assignments. (b) Overlay PDFs of the crystalline mixtures of the (MIL-53)(ZIF-62)(X/Y) series with MIL-53 and ZIF-62. (Inset) ZIF-62 (Zn, red; N, blue; C, gray) with correlation assignments. (c) Simulated PDFs of MIL-53-lp, MIL-53-np, and ZIF-62 using PDFGUI software.[37] Sub-1 Å data are due to the way the solvent occupancies were modeled in the published crystallographic information files used.

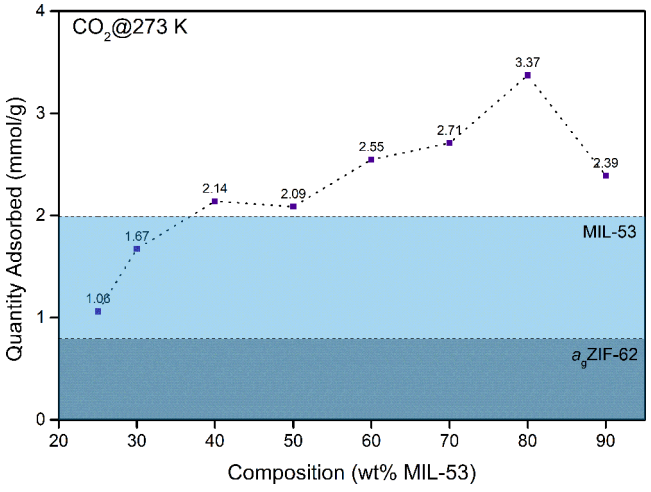

Figure 7. Quantity adsorbed from gas adsorption isotherms for the $(MIL\text{-}53)_x(a_gZIF\text{-}62)_{1-x}$ series at 1 bar using CO_2 gas at 273 K. The quantities adsorbed for samples of activated MIL-53 (MIL-53-np, 1.99 mmol/g) and a_gZIF-62 (0.79 mmol/g) are displayed by light-blue and dark-blue areas, respectively, from Hou et al.[21]

composition was confirmed by NMR, which displayed relevant linker peak integrals varying in proportion to their relative contributions. The crystalline phase contribution of MIL-53 was determined by Rietveld refinement of X-ray diffraction studies, concluding that for MIL-53 loadings up to 60 wt% the only phase observed at room temperature is the metastable MIL-53-lp. Beyond this limit, a percentage of the excluded MIL-53-lp phase proceeds to form MIL-53-np upon cooling. This demonstrates a maximum total loading capacity of between 60 and 70 wt% MIL-53 within a_gZIF-62 in this case. Gas adsorption measurements demonstrate that the maximum effective gas adsorption capacity of the $(MIL\text{-}53)_x(a_gZIF\text{-}62)_{1-x}$ series is around 80 wt%. Here, the MOF-CGC displays a CO_2 adsorption capacity that is 150% the value of pure MIL-53-np. A sample of just 30−40 wt% loading of MIL-53 is expected to adsorb a similar quantity of CO_2 to a sample of pure MIL-53-np. These results show that relatively high loading capacities of crystalline MOFs within a MOF glass can be achieved and provide a first look at the interesting physical properties which may arise as a result.

It is reasonable to propose that the encapsulation and stabilization of the metastable states of a range of breathing MOFs is possible, with the expected crystalline phase at room temperature in the composite being that which is stable at the quenching temperature of the matrix glass.

For the first time, the loading limit of a MOF-CGC system has been identified, opening multiple avenues for potential future research. One such avenue may be the advancement of processing methods, leading to larger incorporations of the active MOF component. Further studies of specific interest are as follows: (i) the diffusion of various guest species into the composite material, (ii) predicting optimum loading limits, (iii) the effects of crystallite size, and (iv) attempts at shaping the bulk products formed. We believe that this may open routes to further functional MOF-CGCs and take advantage of many recent reports of MOF and coordination polymer glass formation.[28−31]

METHODS

Synthesis of MIL-53(Al). Aluminum nitrate nonahydrate (26.00 g, 6.93×10^{-2} mol) and terephthalic acid (5.76 g, 4.96×10^{-2} mol) were dissolved in water (100 mL) and divided into five equal 20 mL aliquots over five Teflon-lined autoclaves. Each reaction vessel was

DOI: 10.1021/jacs.9b07557
J. Am. Chem. Soc. 2019, 141, 15641−15648

placed in a 220 °C preheated oven for 72 h. The white crystalline product was washed with deionized water (3 × 30 mL) and dried overnight at 60 °C.[22]

Synthesis of ZIF-62. Zinc nitrate hexahydrate (3.30 g, 1.11 × 10^{-2} mol) and imidazole (17.82 g, 0.262 mol) were dissolved equally in *N*,*N*-dimethylformamide (150 mL) in two 250 mL screw-top glass jars and stirred for 1 h. Benzimidazole (3.10 g, 2.62 × 10^{-2} mol) was added to the solutions equally and was stirred for another hour before closing the jars tightly and placing in an oven preheated to 130 °C for 48 h. The solutions were allowed to cool to room temperature before filtering and washing with DMF (3 × 30 mL) and DCM (1 × 30 mL) and were placed in an oven at 60 °C to dry overnight to yield a white crystalline powder (3.26 g) with a structure confirmed by PXRD.[32]

Synthesis of (MIL-53)$_x$(a_gZIF-62)$_{1-x}$ MOF-CGCs. Crystalline ZIF-62 and MIL-53-as were ball milled together using a Retsch MM 400 instrument, in appropriate wt% ratios using a 7-mm-diameter stainless steel ball for 15 min, at a frequency of 30 Hz. The mixed powder was pressed in a 13-mm-diameter dye at 0.74 GPa for 1 min. The pellet was then clamped between glass slides, heated to 450 °C at a rate of 20 °C/min, and held for 15 min before being allowed to cool to room temperature under an Ar atmosphere.[21]

X-ray Powder Diffraction. Data were collected on ground samples of the composite materials with a Bruker D8 Advance powder diffractometer using Cu Kα radiation (λ = 1.5418 Å) and a LynxEye position-sensitive detector in Bragg−Brentano (θ–θ) parafocusing geometry at room temperature. Diffraction patterns were recorded at 2θ values of 5−40° with a time/step of 0.75 s over 1724 steps through a 0.012 mm Ni filter. PXRD patterns were analyzed by Rietveld refinements using TOPAS academic (V6) software.[33] Pseudo-Voigt peak shapes were globally refined as a single set of parameters for all scan files. A ninth-order Chebychev polynomial background, a Gaussian background peak accounting for the amorphous background from the ZIF-62 glass, scale factors, unit cell parameters of the MIL-53 structure, and eighth-order spherical harmonics preferred orientation corrections were refined individually for all scans.

Nuclear Magnetic Resonance. NMR measurements were carried out by the NMR Service in The Department of Chemistry, University of Cambridge. Data were recorded on a Bruker 500 MHz DCH cryoprobe spectrometer. Samples were prepared for NMR by digesting each sample in 0.7 mL of a premixed solution of d_6-dimethyl sulfoxide (3.5 mL) and deuterium chloride (1.4 mL), sonicating for 5 min, and allowing 24 h for the MOFs to dissolve.

^{1}H NMR Spectra Assignments. ^{1}H NMR (d_6-DMSO, DCl, 500 MHz) δ_H 7.51 (d, CCHN, imidazole, J = 1.3 Hz), 7.53 (dd, CCHC, benzimidazole, J = 6.2, 3.2 Hz), 7.81 (dd, CCHC, benzimidazole, J = 6.2, 3.2 Hz), 7.95 (s, benzene-1,4-dicarboxylic acid, CCHC), 8.90 (t, NCHN, imidazole, J = 1.25 Hz), 9.43 (s, NCHN, benzimidazole).

Fourier Transform Infrared Absorption. Samples were finely ground and analyzed using a Bruker Tensor 27, scanning wavenumbers of 1−2000 cm^{-1} over 10 scans (Figure S33).

Analytical Scanning Transmission Electron Microscopy (STEM). This technique was used to perform crystallinity mapping based on scanning electron diffraction (SED) and compositional mapping based on X-ray energy-dispersive spectroscopy (EDS). Data were acquired using a JEOL ARM300F at the Diamond Light Source, U.K. fitted with a high-resolution pole piece, cold field emitter, and JEOL spherical aberration correctors in both the probe-forming and image-forming optics. The instrument was operated at 300 kV and aligned in an uncorrected nanobeam configuration and a 10 μm condenser aperture to obtain a convergence semiangle of ∼0.8 mrad and a diffraction-limited probe diameter of <5 nm. Data were acquired with a scan step size of ∼5.2 nm and a camera length of 20 cm. The probe current was ∼2 pA. A Merlin-medipix direct electron detector,[34,35] which is a counting-type detector, was used to record the electron diffraction pattern at each probe position with an exposure time of 1 ms per probe position, leading to a total electron fluence of ∼5 e/Å^2 based on the probe current, exposure time, and assumption of a disklike probe of the diameter above. SED was acquired over a raster pattern comprising 256 × 256 probe positions, and each diffraction pattern comprised 256 × 256 pixels. X-ray energy-dispersive spectroscopy (EDS) maps were acquired from the same regions, following SED acquisition, using a larger probe current obtained using a 150 μm condenser aperture in order to generate sufficient X-ray counts.

SED data were processed using the open source pyXem Python library to find diffraction peaks in every measured diffraction pattern using a difference of Gaussians method, which involves subtracting a blurred version of the diffraction pattern from a less blurred version of the diffraction pattern. EDS data were processed using the open-source HyperSpy Python library to produce maps for each X-ray emission line of interest (Al Kα, Zn Kα), which were extracted by integrating an energy window, background subtracted by linear interpolation from adjacent regions of the spectrum without other X-ray peaks present.

Pair Distribution Function Analysis. Data were obtained at the I15-1 beamline, Diamond Light Source, U.K. (λ = 0.161669 Å, 72 keV). All samples in the series (MIL-53)$_x$(a_gZIF-62)$_{1-x}$ and (MIL-53)(ZIF-62)(X/Y) along with pure samples MIL-53-as, ZIF-62, and a_gZIF-62 and both crystalline and glass-ZIF-62 were finely ground before being packed into sealed 1.17-mm (inner)-diameter borosilicate capillaries. Data were taken of the background, empty capillary, and all samples to a Q_{max} of 26 Å^{-1} with a 10 min acquisition time per sample. Normalized total scattering data were corrected individually using the GudrunX program to obtain the PDF of each sample.[27,36] Predicted patterns were generated using crystallographic information files available online[22] and the PDFGUI software.[37]

Gas Adsorption. CO_2 adsorption measurements were performed on a Micromeritics ASAP 2020 instrument at 273 K (in an ice−water bath) using no less than 20 mg of sample. All samples were degassed at 90 °C for 2 h, followed by 200 °C for another 2 h prior to the adsorption/desorption tests (Figure S34)

Scanning Electron Microscopy. Data were collected on a high-resolution scanning electron microscope, FEI Nova NanoSEM 450. Shards of each monolithic MOF-CGC were coated in chromium prior to imaging.

■ ASSOCIATED CONTENT

Supporting Information

The Supporting Information is available free of charge on the ACS Publications website at DOI: 10.1021/jacs.9b07557.

Scanning electron microscopy (SEM) images, PXRD, synchrotron X-ray total scattering data and corresponding Rietveld refinements, STEM images, structure factors ($S(Q)$), simulated PDF patterns, gas adsorption isotherms, IR, and BET surface areas (PDF)

■ AUTHOR INFORMATION

Corresponding Author

*tdb35@cam.ac.uk

ORCID

Duncan N. Johnstone: 0000-0003-3663-3793
Remo N. Widmer: 0000-0001-7664-4791
Jingwei Hou: 0000-0001-9139-9835
Sean M. Collins: 0000-0002-5151-6360
Thomas D. Bennett: 0000-0003-3717-3119

Notes

The code used to generate crystallinity maps (Johnstone, D. N., et al., pyXem 0.8.0, 2019) is available at 10.5281/zenodo.2807711. The code used to to produce maps for each X-ray emission line of interest (Peña, F. D. L., et al. hyperspy: HyperSpy 1.4.1, 2019) is available at 10.5281/zenodo.1469364.

The authors declare no competing financial interest.

DOI: 10.1021/jacs.9b07557
J. Am. Chem. Soc. 2019, 141, 15641−15648

■ ACKNOWLEDGMENTS

T.D.B. thanks the Royal Society for both a university research fellowship (UF150021) and a research grant (RSG \R1\180395). C.W.A. thanks the Royal Society for a Ph.D. studentship (RG160498) and the Commonwealth Scientific and Industrial Research Council for additional support (C2017/3108). Both J.H. and T.D.B. gratefully acknowledge the EPSRC (EP/R015481/1). A.F.S. acknowledges the EPSRC for a studentship award under the Doctoral Training Programme. A.M.B. acknowledges the Royal Society for funding (RGF\EA\180092) as well as the Cambridge Trust for a Cice Chancellor's Award (304253100). We extend our gratitude to Diamond Light Source, Rutherford Appleton Laboratory, U.K., for access to beamline I15-1 (EE20038-1) and access and support in the use of the electron Physical Science Imaging Centre (EM20195). S.M.C. acknowledges the Henslow Research Fellowship at Girton College, Cambridge. P.A.M. acknowledges funding from the EPSRC (EP/R008779/1) and ExxonMobil.

■ REFERENCES

(1) Furukawa, H.; Cordova, K. E.; O'Keeffe, M.; Yaghi, O. M. The Chemistry and Applications of Metal-Organic Frameworks. *Science* **2013**, *341* (6149), 1230444.

(2) Hönicke, I. M.; Senkovska, I.; Bon, V.; Baburin, I. A.; Bönisch, N.; Raschke, S.; Evans, J. D.; Kaskel, S. Balancing Mechanical Stability and Ultrahigh Porosity in Crystalline Framework Materials. *Angew. Chem.−Int. Ed.* **2018**, *57* (42), 13780−13783.

(3) Farha, O. K.; Eryazici, I.; Jeong, N. C.; Hauser, B. G.; Wilmer, C. E.; Sarjeant, A. A.; Snurr, R. Q.; Nguyen, S. T.; Yazaydin, A. Ö.; Hupp, J. T. Metal-Organic Framework Materials with Ultrahigh Surface Areas: Is the Sky the Limit? *J. Am. Chem. Soc.* **2012**, *134* (36), 15016−15021.

(4) Kim, H.; Yang, S.; Rao, S. R.; Narayanan, S.; Kapustin, E. A.; Furukawa, H.; Umans, A. S.; Yaghi, O. M.; Wang, E. N. Water Harvesting from Air with Metal-Organic Frameworks Powered by Natural Sunlight. *Science* **2017**, *356*, 430−434.

(5) Ma, S.; Zhou, H. C. Gas Storage in Porous Metal-Organic Frameworks for Clean Energy Applications. *Chem. Commun.* **2010**, *46* (1), 44−53.

(6) Li, J.-R.; Kuppler, R. J.; Zhou, H.-C. Selective Gas Adsorption and Separation in Metal-Organic Frameworks. *Chem. Soc. Rev.* **2009**, *38* (5), 1477−1504.

(7) Kreno, L. E.; Leong, K.; Farha, O. K.; Allendorf, M.; Van Duyne, R. P.; Hupp, J. T. Metal-Organic Framework Materials as Chemical Sensors. *Chem. Rev.* **2012**, *112* (2), 1105−1125.

(8) Hindocha, S.; Poulston, S. Study of the Scale-up, Formulation, Ageing and Ammonia Adsorption Capacity of MIL-100(Fe), Cu-BTC and CPO-27(Ni) for Use in Respiratory Protection Filters. *Faraday Discuss.* **2017**, *201*, 113−125.

(9) Tian, T.; Zeng, Z.; Vulpe, D.; Casco, M. E.; Divitini, G.; Midgley, P. A.; Silvestre-Albero, J.; Tan, J. C.; Moghadam, P. Z.; Fairen-Jimenez, D. A Sol-Gel Monolithic Metal-Organic Framework with Enhanced Methane Uptake. *Nat. Mater.* **2018**, *17* (2), 174−179.

(10) Sumida, K.; Liang, K.; Reboul, J.; Ibarra, I. A.; Furukawa, S.; Falcaro, P. Sol-Gel Processing of Metal-Organic Frameworks. *Chem. Mater.* **2017**, *29* (7), 2626−2645.

(11) Lohe, M. R.; Rose, M.; Kaskel, S. Metal-Organic Framework (MOF) Aerogels with High Micro- and Macroporosity. *Chem. Commun.* **2009**, No. 40, 6056−6058.

(12) Widmer, R. N.; Lampronti, G. I.; Kunz, B.; Battaglia, C.; Shepherd, J. H.; Redfern, S. A. T.; Bennett, T. D. Manufacturing Macroporous Monoliths of Microporous Metal−Organic Frameworks. *ACS Appl. Nano Mater.* **2018**, *1* (2), 497−500.

(13) Rubio-Martinez, M.; Avci-Camur, C.; Thornton, A. W.; Imaz, I.; Maspoch, D.; Hill, M. R. New Synthetic Routes towards MOF Production at Scale. *Chem. Soc. Rev.* **2017**, *46* (11), 3453−3480.

(14) Zhu, Q.-L.; Xu, Q. Metal-Organic Framework Composites. *Chem. Soc. Rev.* **2014**, *43* (16), 5648−5512.

(15) Denny, M. S., Jr.; Moreton, J. C.; Benz, L.; Cohen, S. M. Metal−Organic Frameworks for Membrane-Based Separations. *Nat. Rev. Mater.* **2016**, *1*, 16078.

(16) Park, K. S.; Ni, Z.; Côté, A. P.; Choi, J. Y.; Huang, R.; Uribe-Romo, F. J.; Chae, H. K.; O'Keeffe, M.; Yaghi, O. M. Exceptional Chemical and Thermal Stability of Zeolitic Imidazolate Frameworks. *Proc. Natl. Acad. Sci. U. S. A.* **2006**, *103* (27), 10186−10191.

(17) Tian, Y. Q.; Zhao, Y. M.; Chen, Z. X.; Zhang, G. N.; Weng, L. H.; Zhao, D. Y. Design and Generation of Extended Zeolitic Metal-Organic Frameworks (ZMOFs): Synthesis and Crystal Structures of Zinc(II) Imidazolate Polymers with Zeolitic Topologies. *Chem. - Eur. J.* **2007**, *13* (15), 4146−4154.

(18) Arhangelskis, M.; Katsenis, A. D.; Novendra, N.; Akimbekov, Z.; Gandrath, D.; Marrett, J. M.; Ayoub, G.; Morris, A. J.; Farha, O. K.; Friščić, T.; Navrotsky, A. Theoretical Prediction and Experimental Evaluation of Topological Landscape and Thermodynamic Stability of a Fluorinated Zeolitic Imidazolate Framework. *Chem. Mater.* **2019**, *31*, 3777−3783.

(19) Gaillac, R.; Pullumbi, P.; Beyer, K. A.; Chapman, K. W.; Keen, D. A.; Bennett, T. D.; Coudert, F.-X. Liquid Metal−Organic Frameworks. *Nat. Mater.* **2017**, *16*, 1149−1155.

(20) Bennett, T. D.; Yue, Y.; Li, P.; Qiao, A.; Tao, H.; Greaves, N. G.; Richards, T.; Lampronti, G. I.; Redfern, S. A. T.; Blanc, F.; Farha, O. K.; Hupp, J. T.; Cheetham, A. K.; Keen, D. A. Melt-Quenched Glasses of Metal-Organic Frameworks. *J. Am. Chem. Soc.* **2016**, *138* (10), 3484−3492.

(21) Hou, J.; Ashling, C. W.; Collins, S. M.; Krajnc, A.; Zhou, C.; Longley, L.; Johnstone, D. N.; Chater, P. A.; Li, S.; Coulet, M.-V.; Llewellyn, P. L.; Coudert, F.-X.; Keen, D. A.; Midgley, P. A.; Mali, G.; Chen, V.; Bennett, T. D. Metal-Organic Framework Crystal-Glass Composites. *Nat. Commun.* **2019**, *10*, 2580.

(22) Loiseau, T.; Serre, C.; Huguenard, C.; Fink, G.; Taulelle, F.; Henry, M.; Bataille, T.; Férey, G. A Rationale for the Large Breathing of the Porous Aluminum Terephthalate (MIL-53) Upon Hydration. *Chem. - Eur. J.* **2004**, *10* (6), 1373−1382.

(23) Mounfield, W. P.; Walton, K. S. Effect of Synthesis Solvent on the Breathing Behavior of MIL-53(Al). *J. Colloid Interface Sci.* **2015**, *447*, 33−39.

(24) Bennett, T. D.; Goodwin, A. L.; Dove, M. T.; Keen, D. A.; Tucker, M. G.; Barney, E. R.; Soper, A. K.; Bithell, E. G.; Tan, J. C.; Cheetham, A. K. Structure and Properties of an Amorphous Metal-Organic Framework. *Phys. Rev. Lett.* **2010**, *104* (11), 2−5.

(25) Billinge, S. J. L.; Dykhne, T.; Juh, P.; Taylor, R.; Florence, J. Characterisation of Amorphous and Nanocrystalline Molecular Materials by Total Scattering. *CrystEngComm* **2010**, *12*, 1366−1368.

(26) Chapman, K. W.; Sava, D. F.; Halder, G. J.; Chupas, P. J.; Nenoff, T. M. Trapping Guests within a Nanoporous Metal-Organic Framework through Pressure-Induced Amorphization. *J. Am. Chem. Soc.* **2011**, *133* (46), 18583−18585.

(27) Soper, A. K. *GudrunN and GudrunX: Programs for Correcting Raw Neutron and X-ray Diffraction Data to Differential Scattering Cross Section*; Tech. Rep. RAL-TR-2011-2013; Rutherford Appleton Laboratory Technical Report, Oxfordshire, 2011.

(28) Umeyama, D.; Horike, S.; Inukai, M.; Itakura, T.; Kitagawa, S. Reversible Solid-to-Liquid Phase Transition of Coordination Polymer Crystals. *J. Am. Chem. Soc.* **2015**, *137* (2), 864−870.

(29) Kimata, H.; Mochida, T. Crystal Structures and Melting Behaviors of 2−D and 3−D Anionic Coordination Polymers Containing Organometallic Ionic Liquid Components. *Chem. - Eur. J.* **2019**, *25*, 10111.

(30) Zhao, Y.; Lee, S. Y.; Becknell, N.; Yaghi, O. M.; Angell, C. A. Nanoporous Transparent MOF Glasses with Accessible Internal Surface. *J. Am. Chem. Soc.* **2016**, *138* (34), 10818−10821.

DOI: 10.1021/jacs.9b07557
J. Am. Chem. Soc. 2019, 141, 15641−15648

(31) Frentzel-Beyme, L.; Kloß, M.; Pallach, R.; Salamon, S.; Moldenhauer, H.; Landers, J.; Wende, H.; Debus, J.; Henke, S. Porous Purple Glass-a Cobalt Imidazolate Glass with Accessible Porosity from a Meltable Cobalt Imidazolate Framework. *J. Mater. Chem. A* **2019**, *7* (3), 985−990.
(32) Qiao, A.; Bennett, T. D.; Tao, H.; Krajnc, A.; Mali, G.; Doherty, C. M.; Thornton, A. W.; Mauro, J. C.; Greaves, G. N.; Yue, Y. A Metal-Organic Framework with Ultrahigh Glass-Forming Ability. *Sci. Adv.* **2018**, *4* (3), eaao6827.
(33) Coelho, A. *Topas Academia v6*; Coelho Software: Brisbane, Australia, 2007.
(34) Nederlof, I.; Van Genderen, E.; Li, Y. W.; Abrahams, J. P. A Medipix Quantum Area Detector Allows Rotation Electron Diffraction Data Collection from Submicrometre Three-Dimensional Protein Crystals. *Acta Crystallogr., Sect. D: Biol. Crystallogr.* **2013**, *69* (7), 1223−1230.
(35) Mir, J. A.; Clough, R.; MacInnes, R.; Gough, C.; Plackett, R.; Shipsey, I.; Sawada, H.; MacLaren, I.; Ballabriga, R.; Maneuski, D.; O'Shea, V.; McGrouther, D.; Kirkland, A. I. Characterisation of the Medipix3 Detector for 60 and 80 KeV Electrons. *Ultramicroscopy* **2017**, *182*, 44−53.
(36) Soper, A. K.; Barney, E. R. Extracting the Pair Distribution Function from White-Beam X-Ray Total Scattering Data. *J. Appl. Crystallogr.* **2011**, *44* (4), 714−726.
(37) Farrow, C. L.; Juhas, P.; Liu, J. W.; Bryndin, D.; Boin, E. S.; Bloch, J.; Proffen, T.; Billinge, S. J. L. PDFfit2 and PDFgui: Computer Programs for Studying Nanostructure in Crystals. *J. Phys.: Condens. Matter* **2007**, *19* (33), 335219.

DOI: 10.1021/jacs.9b07557
J. Am. Chem. Soc. 2019, 141, 15641−15648